Experimental Study on Full-Surface Buckling of Variable Curvature Cylindrical Shell Using Multi-camera 3D-DIC System

*LI Xin, SUN Wei**

College of Aerospace Engineering, Nanjing University of Aeronautics and Astronautics, Nanjing 210016, P. R. China

(Received 30 August 2024; revised 8 October 2024; accepted 15 October 2024)

Abstract: To achieve full-surface strain measurement of variable curvature objects, a 360° 3D digital image correlation (DIC) system is proposed. The measurement system consists of four double-camera systems, which capture the object's entire surface from multiple angles, enabling comprehensive full-surface measurement. To increase the stitching quality, a hierarchical coordinate matching method is proposed. Initially, a 3D rigid body calibration auxiliary block is employed to track motion trajectory, which enables preliminary matching of four 3D-DIC sub-systems. Subsequently, secondary precise matching is performed based on feature points on the test specimen's surface. Through the hierarchical coordinate matching method, the local 3D coordinate systems of each double-camera system are unified into a global coordinate system, achieving 3D surface reconstruction of the variable curvature cylindrical shell, and error analysis is conducted on the results. Furthermore, axial compression buckling experiment is conducted to measure the displacement and strain fields on the cylindrical shell's surface. The experimental results are compared with the finite element analysis, validating the accuracy and effectiveness of the proposed multi-camera 3D-DIC measuring system.

Key words: 360° 3D digital image correlation (DIC); hierarchical coordinate matching method; full-field 3D deformation measurement; variable curvature cylindrical shell

CLC number: TP301 **Document code:** A **Article ID:** 1005-1120(2024)05-0589-10

0 Introduction

Digital image correlation (DIC) method is a non-contact modern optical measurement technique. Due to its advantages, such as good environmental adaptability, full-field measurement, and a wide range of applications, it has been widely used in various scientific and engineering fields, including aerospace, civil engineering, materials science, biomedical engineering, manufacturing, manufacturing, welding, and so on[1]. In these fields, buckling problem is consistently a significant topic. Validating buckling response through simulation and experimentation, engineers can predict and prevent potential failure modes, ensuring that the structure can maintain its performance even after prolonged use. For example, the design of cylindrical shells for spacecraft must remain stable under extreme pressures and temperatures, and buckling analysis helps ensure that the structure can work properly under these conditions[2]. Overall, the study of buckling problem is crucial for enhancing the safety, economy, and reliability of structural design.

For objects with variable curvature surface, anisotropy, or asymmetric shape, it is unreasonable to conduct full-field analysis only through a certain surface. In order to fulfill the deformation measurement of the full surface of the measured object, the effective field of view of the camera must cover the full surface of the object. However, the conventional 3D DIC using two cameras can only obtain a certain surface of the measured object, which cannot meet the requirements of full surface measurement[3]. To meet this requirement, researchers have proposed a

*Corresponding author, E-mail address: nancysun@nuaa.edu.cn.

How to cite this article: LI Xin, SUN Wei. Experimental study on full-surface buckling of variable curvature cylindrical shell using multi-camera 3D-DIC system[J]. Transactions of Nanjing University of Aeronautics and Astronautics, 2024, 41(5): 589-598.

http://dx.doi.org/10.16356/j.1005-1120.2024.05.004

series of methods. Rotating a single camera around the test object for shooting is a low-cost and space-saving method. Spera et al.[4] sequentially moved a single camera through seven fixed positions in order to cover the desired angle of vision to realize the full-field deformation measurement of porcine intervertebral disc. Genovese et al.[5] developed a single-camera 3D-DIC system, where the camera was mounted on a designed rotary bearing ring to rotate around the sample and capture images, and completed a 360° surface and deformation measurement of a Grade X65 steel sample under tensile loading. In order to solve the problem of image acquisition and processing in the full-field displacement measurement of large-scale structure, Guo et al.[6] proposed a large-scale structural displacement field calculation framework, which realizes the imaging and splicing of large structures with a single camera and automatic rotation platform. Conversely, the camera can be fixed in place while rotating the object for measurement. Badel et al.[7] placed arterial wall samples on a rotary table for rotating shooting and presented an inverse approach based on a finite element model to determine the local distribution of residual strain and stress from full-field digital image correlation measurements. Heuer et al.[8] placed an intervertebral disc on a rotating arm and performed imaging using a laser scanner to investigate the annular fiber strains and disc bulging under simple and complex spinal loads. Although the two methods mentioned above are simple and quick to operate, they are merely suitable for situations where no load is applied. When it is necessary to apply a load to the specimen, one must either pause the loading at specific moments or wait until the specimen reaches a stable state such as destruction after loading to conduct full-field measurements. In other words, the above two methods can only meet static or quasi-static measurement requirements.

In order to conduct dynamic measurement of the full field , the scholars have proposed the mirror-assisted DIC method[9-10] and multi-camera DIC method[11-13]. Chen et al.[14] used a pair of synchronous cameras and two planar mirrors to achieve the dynamic measurement of full-field shape and deformation of human parts, showing the great potential of DIC for skin biomechanical research. Zhu et al.[15] used two planar mirrors and a single camera attached with a four-mirror adapter to capture stereo images of the front and rear surfaces of a test object, achieving panoramic/dual-surface shape and deformation measurements. Xie et al.[16] established a cost-effective and easy-to-implement mirror-assisted multi-view high-speed DIC method for the dynamic deformation measurement of the full-field, and verified the effectiveness and accuracy of the established system through modal test of a cantilever aluminum sheet. Compared with the first and second methods mentioned above, the mirror-assisted DIC method still maintains a relatively cost-effective and compact space while meeting the requirements of dynamic measurement. However, during the experimental process, the planar mirror may introduce extra optical distortion and reflection error, which requires additional correction procedure. Moreover, this method requires to simultaneously capture both the front image of the subject and the back image reflected through the mirror. When the test subject is large, the depth of field problem may lead to lower image sharpness, which may affect the measurement accuracy. The multi-camera DIC method, which capture images simultaneously from different angles with multiple cameras, can provide more comprehensive, accurate, and reliable full-field measurement data. It is also the most widely used method in engineering applications. Li et al.[17] set up a multi-camera DIC system used to measure the whole-field thickness strain, capturing the full-field deformation and thickness strains throughout the entire stretching process. Genovese et al.[18] designed, set up, and validated a four-camera panoramic-DIC system for testing murine arteries and a multi-biprism DIC system for testing human arteries. Both systems enable dynamic 360° measurements with refraction correction over the entire surface of submerged samples in their native geometries. Zhu et al.[19] established a multi-camera array system and proposed a reliability-guided frequency-domain-based DIC method, addressing the limitations of traditional DIC measurement methods in full-field modal measurement. They validated the method's accuracy by conducting the modal test of

a solar panel using a four-camera system.

However, the drawbacks of multi-camera DIC measurement methods include high equipment cost, larger space requirements during experiments, and potential interference among camera systems, such as reflections or occlusions. Careful planning of the equipment layout before the experiment is necessary to avoid these issues. Additionally, addressing the unification of coordinate systems and data stitching among the camera subsystems is a critical challenge for multi-camera DIC measurement methods.

In this paper, a multi-camera 3D-DIC system is built for the cylindrical shell of variable curvature. In order to accommodate the slender shape of the specimen, the two cameras within each subsystem are arranged vertically to make full use of the camera resolution and improve the overlapping field of view. Through a synchronous controller triggered by hardware, the cameras synchronously capture images from four different angles[20]. A hierarchical coordinate matching method is proposed to achieve the unification of the coordinate systems of all camera systems and perform initial point cloud matching by tracking the motion trajectory of a 3D rigid calibration block using speckle information. Secondly, point cloud matching is completed based on the gray-scale feature of surface characteristic points, resulting in obtaining a complete and accurate topography pattern. Ultimately, full surface compression buckling test of variable curvature cylindrical shell is validated[21-23].

1 Hierarchical Coordinate Matching Method

1.1 Multi-camera calibration method based on rigid body motion

The first step of this method is multi-camera calibration method based on rigid body motion[24]. Select a rigid block of the same size as the specimen and make speckle patterns on its surrounding surface. Determine the relative extrinsic parameters between subsystems by moving and capturing the rigid body calibration block. Compared to traditional multi-camera calibration methods based on overlapping fields of view, the multi-camera calibration method based on rigid body motion does not require overlapping fields of view between camera systems, and it is very convenient to make a calibration block. This method simplifies multi-camera calibration operations and has strong applicability.

Step 1 The dot calibration board is used to calibrate each camera system, and obtain the internal parameters and external parameters of each camera in each system[25].

This step is fundamental for unifying local coordinate systems of all camera systems. Good calibration ensures that the projection errors calculated by each subsystem are minimized, which guarantees accurate tracking of the rigid body motion trajectory to achieve precise multi-view matching.

Step 2 In the previous calibration step, the external parameters of each camera are relative to the local coordinate system of the camera system. It is also necessary to unify all local coordinate systems to the global coordinate system using rigid body calibration block.

A series of rigid motions are applied to the calibration block in the center of the field of view, and each camera system simultaneously captures the different surfaces of the calibration block. In the schematic diagram of the multi-camera system in Fig.1, the geometric transformation relationship between camera systems is shown. In Fig.1, O_{w1}-$X_{w1}Y_{w1}Z_{w1}$ represents the auxiliary world coordinate system corresponding to the front surface of the calibration block taken by the first camera system (sys-1). O_{c1}-$X_{c1}Y_{c1}Z_{c1}$ and O-u_1v_1 are the local coordinate system and pixel coordinate system of camera system 1, corresponding to the auxiliary world coordinate system O_{w1}-$X_{w1}Y_{w1}Z_{w1}$. Similarly, O_{wn}-$X_{wn}Y_{wn}Z_{wn}$ represents the auxiliary world coordinate system corresponding to the surface of the calibration block captured by the nth system (sys-n), and the expressions for other coordinate systems are also similar. Based on the rigid feature of the calibration block, which do not deform during movement, these auxiliary world coordinate systems are situated within the same global coordinate system established by the rigid body calibration block. The binocular stereovision technique is utilized to reconstruct the 3D world coordinates of each surface point of the rigid

body object, while simultaneously solving the vector motion trajectory of each surface in relation to the center of gravity[26]. Additionally, the iterative closest point (ICP) algorithm[27] is employed in conjunction with the least square method to obtain the rotation matrix and translation matrix between distinct camera local coordinate systems.

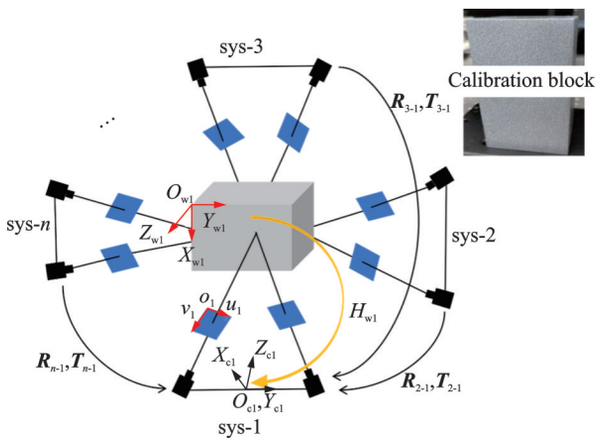

Fig.1 Schematic diagram of geometric transformations in the multi-camera 3D-DIC system

Here, the camera coordinate system of sys-1 is used as the reference global coordinate system. Thus, the rotation matrix $\boldsymbol{R}_{i-1}$ and translation matrix $\boldsymbol{T}_{i-1}$ of any system i relative to the sys-1 can be determined, ultimately achieving global calibration of multiple cameras. The expression for converting coordinates from other camera local coordinate systems to the reference global coordinate system is

$$\boldsymbol{Q}_{\mathrm{c}}^{i-1}=\boldsymbol{R}_{i-1}(\boldsymbol{H}_{\mathrm{w}i}\boldsymbol{Q}_{\mathrm{c}}^{i})+\boldsymbol{T}_{i-1}\quad i=1,2,\cdots,n \tag{1}$$

where $\boldsymbol{Q}_{\mathrm{c}}^{i-1}$ representing the coordinate of the spatial point within the local coordinate system of system i is transformed into the world coordinate system. $\boldsymbol{R}_{i-1}$ and $\boldsymbol{T}_{i-1}$ are the rotation matrix and translation matrix from local coordinate system of system i to global coordinate system. $\boldsymbol{H}_{\mathrm{w}i}$ is the projection transformation matrix between the pixel coordinate system and the local coordinate system of the camera system n, which has been obtained through calibration in Step 1. $\boldsymbol{Q}_{\mathrm{c}}^{i}$ is the pixel coordinate of the center of a selected subset in the pixel coordinate system of camera 0, which is the main camera in the system i. $\boldsymbol{H}_{\mathrm{w}i}\boldsymbol{Q}_{\mathrm{c}}^{i}$ is the 3D coordinate of the spatial point calculated in local coordinate system of system i. After converting all local coordinate systems to the reference global coordinate system, the complete 3D topography of the specimen can be obtained.

1.2 Point cloud matching based on feature point grayscale information

The multi-camera calibration method based on rigid body motion can perform the calibration between multiple camera systems simultaneously, reducing the operation steps and avoiding the error transmission between systems. However, this method is affected by factors such as the flatness of the rigid body surface, calibration errors, environmental noise, and lighting conditions, so there are still certain errors in the registration. Therefore, further matching of the point cloud data after the coordinate system is required. As shown in Fig.2, three characteristic points are randomly distributed at each quarter position of the specimen surface, and the gray values within these points gradually distribute along the radius. The spatial correspondence is established from these characteristic points, and the rotation matrix and the translation matrix between the point clouds acquired by each system are obtained by the singular value decomposition (SVD) method.

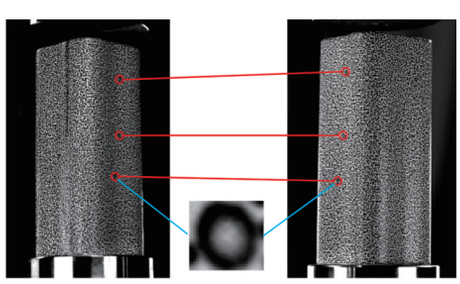

Fig.2 Schematic diagram of feature point distribution and point set matching

The multi-camera system captures images of the specimen from four different angles, three non-collinear feature points can be found within the overlapping area[28] obtained by any adjacent two-camera systems. Since the grayscale values of feature points decrease gradually along the radial direction, meaning the grayscale value is maximum at the center of the point, identifying the point with the highest grayscale value allows for locating the center of the feature point. By using the traversal comparison algorithm, each pixel point's grayscale value within

the feature points is compared individually to accurately identify the circle's center coordinates, and spatial correspondences are established based on these coordinates.

Due to the inability to set the step size to one pixel during calculation, which requires a large amount of computational cost and may cause excessive sensitivity to noise, resulting in a decrease in accuracy, when the center coordinates of feature points are identified, their corresponding 3D coordinates may not be directly obtained. In this case, interpolation method is used to obtain their 3D coordinates through the nearest data points around them. The centers of the three feature points in the left picture of Fig.2 are defined as the point set to be registered $\boldsymbol{P}\{\boldsymbol{p}_i|\boldsymbol{p}_i\in\boldsymbol{P}, i=1,2,3\}$, and the centers of the three feature points in the right picture are defined as the target point sets $\boldsymbol{Q}\{\boldsymbol{q}_i|\boldsymbol{q}_i\in\boldsymbol{Q}, i=1,2,\cdots,3\}$. The matching of overlapping areas is to obtain the coordinate transformation relationship between two-point sets, namely the rotation matrix $\boldsymbol{R}$ and the displacement matrix $\boldsymbol{T}$. After obtaining the corresponding point sets, the rigid transformation matrices $\boldsymbol{R}$ and $\boldsymbol{T}$ can be obtained by minimizing the objective function, shown as

$$J=\sum_{i=1}^{k}\|\boldsymbol{q}_i-(\boldsymbol{R}\boldsymbol{p}_i+\boldsymbol{T})\|^2 \tag{2}$$

where k is the number of matching points. Assuming the least-squares solutions are $\boldsymbol{R}'$ and $\boldsymbol{T}'$, then the centroids of $\boldsymbol{q}_i'=\boldsymbol{R}'\boldsymbol{p}_i+\boldsymbol{T}'$ and $\boldsymbol{Q}$ are the same, i.e. $\overline{\boldsymbol{Q}}=\overline{\boldsymbol{Q}'}$, where $\overline{\boldsymbol{Q}}$ and $\overline{\boldsymbol{Q}'}$ are as follows

$$\overline{\boldsymbol{Q}}=\frac{1}{k}\sum_{i=1}^{k}\boldsymbol{q}_i,\quad \overline{\boldsymbol{Q}'}=\frac{1}{k}\sum_{i=1}^{k}\boldsymbol{q}_i' \tag{3}$$

The centroid $\bar{\boldsymbol{P}}$ of point set $\boldsymbol{P}$ is

$$\overline{\boldsymbol{P}}=\frac{1}{k}\sum_{i=1}^{k}\boldsymbol{p}_i \tag{4}$$

Then, we have

$$\boldsymbol{d}_i=\boldsymbol{p}_i-\overline{P},\quad \boldsymbol{d}_i^*=\boldsymbol{q}_i-\overline{\boldsymbol{Q}} \tag{5}$$

The objective function now can be rewritten as

$$J=\sum_{i=1}^{k}\|\boldsymbol{d}_i^*-\boldsymbol{R}\boldsymbol{d}_i\|^2 \tag{6}$$

Then $\boldsymbol{J}$ is expanded into

$$J=\sum_{i=1}^{k}(\boldsymbol{d}_i^*-\boldsymbol{R}\boldsymbol{d}_i)^{\mathrm{T}}(\boldsymbol{d}_i^*-\boldsymbol{R}\boldsymbol{d}_i)=$$

$$\sum_{i=1}^{k}(\boldsymbol{d}_i^{*\mathrm{T}}\boldsymbol{d}_i^*-\boldsymbol{d}_i^{*\mathrm{T}}\boldsymbol{R}\boldsymbol{d}_i-\boldsymbol{d}_i^{\mathrm{T}}\boldsymbol{R}^{\mathrm{T}}\boldsymbol{d}_i^*+\boldsymbol{d}_i^{\mathrm{T}}\boldsymbol{R}^{\mathrm{T}}\boldsymbol{R}\boldsymbol{d}_i)=$$

$$\sum_{i=1}^{k}(\boldsymbol{d}_i^{*\mathrm{T}}\boldsymbol{d}_i^*+\boldsymbol{d}_i^{\mathrm{T}}\boldsymbol{d}_i-2\boldsymbol{d}_i^{*\mathrm{T}}\boldsymbol{R}\boldsymbol{d}_i) \tag{7}$$

To minimize $\boldsymbol{J}$, it is necessary to take the derivative of $\boldsymbol{J}$ to obtain $\boldsymbol{J}'$ and maximize it.

$$J'=\sum_{i=1}^{k}\boldsymbol{d}_i^{*\mathrm{T}}\boldsymbol{R}\boldsymbol{d}_i=\mathrm{tr}\left(\sum_{i=0}^{k}\boldsymbol{R}\boldsymbol{d}_i\boldsymbol{d}_i^{*\mathrm{T}}\right)=\mathrm{tr}(\boldsymbol{R}\boldsymbol{H}) \tag{8}$$

where $\boldsymbol{H}$ is a third-order square matrix, shown as

$$\boldsymbol{H}=\sum_{i=1}^{k}\boldsymbol{d}_i\boldsymbol{d}_i^{*\mathrm{T}} \tag{9}$$

Matrix $\boldsymbol{H}$ is decomposed by SVD, shown as

$$\boldsymbol{H}=\boldsymbol{U}\boldsymbol{\Lambda}\boldsymbol{V}^{\mathrm{T}} \tag{10}$$

Let

$$\boldsymbol{X}=\boldsymbol{V}\boldsymbol{U}^{\mathrm{T}}$$

Then, we have

$$\boldsymbol{X}\boldsymbol{H}=\boldsymbol{V}\boldsymbol{U}^{\mathrm{T}}\boldsymbol{U}\boldsymbol{\Lambda}\boldsymbol{V}^{\mathrm{T}}=\boldsymbol{V}\boldsymbol{\Lambda}\boldsymbol{V}^{\mathrm{T}} \tag{11}$$

It can be seen that $\boldsymbol{XH}$ is a symmetric positive definite matrix, so there is $\mathrm{tr}(\boldsymbol{XH})\geqslant\mathrm{tr}(\boldsymbol{BXH})$ for any third-order orthogonal matrix $\boldsymbol{B}$. Thus, all third-order orthogonal matrices, only when the determinant of $\boldsymbol{X}$ is close to or equal to 1 (transformed to make it completely coincident), then the rotation matrix $\boldsymbol{R}=\boldsymbol{X}$. The translation matrix is

$$\boldsymbol{T}=\overline{\boldsymbol{Q}}-\boldsymbol{R}\frac{1}{k}\sum_{i=1}^{k}\boldsymbol{p}_i \tag{12}$$

2 Experiment

2.1 Experimental preparation and arrangement

The corrugated surface of a variable curvature cylindrical shell is obtained by superimposing a sine curve on a reference circle. The expression for a sine curve can be written as $\rho=22.5+3\sin(4\theta)$, where the unit is mm, ρ and θ are the polar coordinates of the point on the curve, and 22.5 mm is the radius of the reference circle. Fig.3 shows the sectional shape of the shell, with a thickness of 4 mm.

The variable curvature cylindrical shell specimen is generated using soft adhesive material by 3D printing technology. In order to reduce the reflective effect on the surface of the variable curvature cylindrical shell, the specimen on the left is treated with matte white paint (Fig.4(a)). A layer of matte

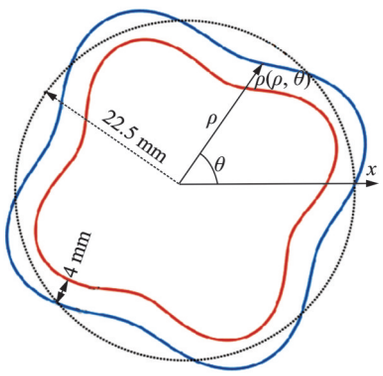

Fig.3 Sectional shape of the shell

white paint is uniformly sprayed on the surface of the specimen, which can also improve the contrast of the obtained image. During the process, it is necessary to avoid the phenomenon of excessive paint film thickness and paint film sagging, which will affect the accuracy of subsequent experiments. After the paint is completely dry and cured, a digital speckle pattern is generated by using the software Speckle Generator and prefabricated on transfer paper. Then, the transfer paper is firmly pressed onto the surface of the specimen and evenly wetted with a wet wipe, which is called hydro transfer printing, allowing the entire speckle pattern, including feature points, to adhere to the surface of the specimen. The speckle is shown in Fig.4(b).

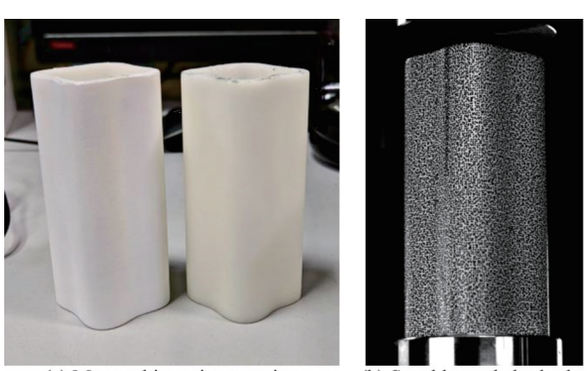

(a) Matte white paint spraying (b) Speckle made by hydro transfer printing

Fig.4 Surface pretreatment of specimen

The experimental setup comprised eight Basler industrial cameras (model acA4112-30 μm), each possessing a resolution of 4 096 pixel ×3 008 pixel and capable of capturing 300 frame/s. On the premise of meeting the measurement requirement of a 360° full surface field of view, in order to improve the field of view utilization of each camera system and simplify the experimental steps, this paper adopts the arrangement[29] shown in Fig.5 for the multi camera system.

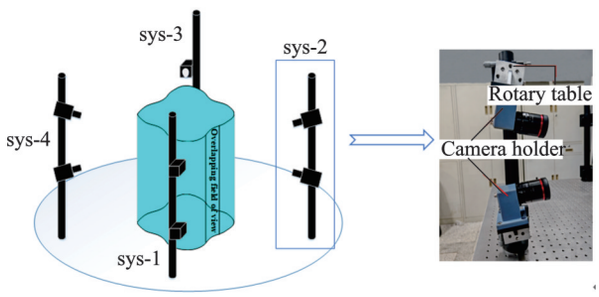

Fig.5 Camera arrangement

The eight cameras are divided into four pairs, each pair forming a stereo DIC measurement system. The front, left, right, and rear surfaces of the specimen are then photographed by the four measuring systems. Due to the long length of the specimen, as well as the large curvature and variable curvature characteristics, in order to fully utilize the resolution of the cameras and improve the overlapping field of view between them, the two cameras in each system are arranged vertically and fixed on a pillar. By vertically arranging the cameras, the overlapping field of view of the two systems can be equivalent to the field of view of a single camera by adjusting the pitch angle.

Fig.6 presents the experimental setup employed for the variable curvature cylindrical shell specimen. The cameras adopt the arrangement shown in Fig.5, with four blue light sources with biased filters symmetrically placed between each system, and the brightness of the light sources is consistent to ensure uniform illumination of the specimen. Through the synchronous controller, eight cameras are synchronized for image acquisition in hardware triggered mode. The specimen is loaded by using a hand-operated pressure testing machine with a range of 1 000 N and a resolution of 1 N, which can display the load size in real-time. The load is used by rotating the joystick of the hand-operated pressure testing machine slowly and continuously. Whenever the load reaches a series of fixed values, the camera is automatically controlled to capture pictures, and then the joystick can be allowed to be rotated continuously.

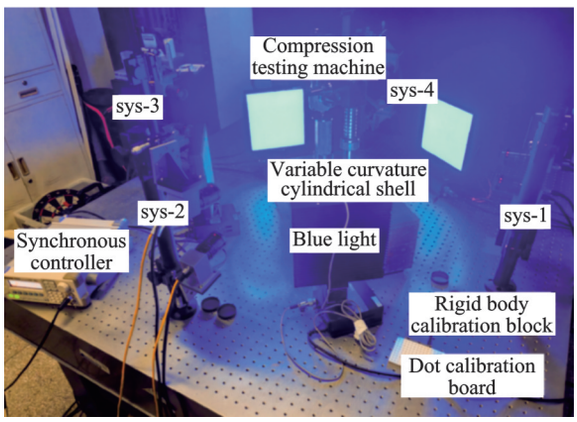

Fig.6 Experimental diagram of compression measurement of variable curvature cylindrical shell

2.2 Experimental result

2.2.1 360° 3D shape measurement and matching

The present study involves the selection of the region of interest (ROI) from the four camera systems. The 3D coordinates of the ROI are then calculated using the conventional 3D-DIC system. The subset and step are determined as 57 pixel × 57 pixel and 11 pixel based on image quality and noise level. Then, based on the multi-camera calibration method based on rigid body motion, the positional relationships between the four camera systems were obtained. The point cloud of the four systems were unified in the same global coordinate system, and the complete 3D shape of the variable curvature cylindrical shell specimen is obtained, as shown in Fig.7.

As can be seen, the splicing is not continuous, which is caused by a series of factors such as calibration error, surface flatness of rigid body, environmental noise, and imaging quality. Therefore, further precise matching is required.

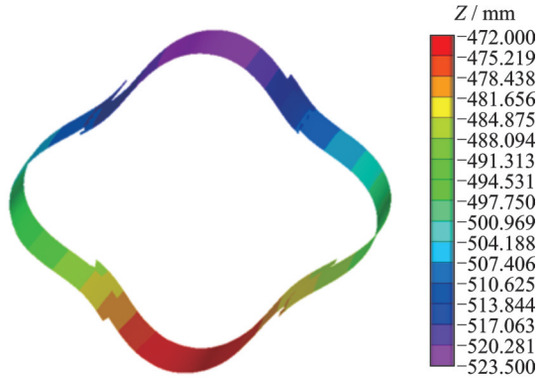

Fig.7 3D shape diagram of the variable curvature cylindrical shell after multi-camera calibration

Based on the gray-scale information of the feature points, the central coordinates of the feature points can be obtained. These feature points are in the region of overlap between different camera systems and own the same world coordinates. By using the SVD method, the transformation relationship between corresponding point pairs based on the local coordinate values is calculated, which is applied to the point cloud to be registered. The coordinate system of sys-1 is used as global coordinate system for point cloud matching. Since sys-2 and sys-4 both have overlapping fields of view with sys-1, the data of the point cloud of sys-2 and sys-4 can be corrected directly by the conversion matrix calculated using the corresponding point pairs. However, there is no overlapping area between sys-3 and sys-1, so it is impossible to directly correct syst-3. Therefore, the data of the point cloud of sys-3 must be corrected to the corrected sys-2 or sys-4 first, and then corrected to sys-1. The point cloud matching between adjacent systems is shown in Fig.8, and the corrected 3D shape diagram is shown in Fig.9.

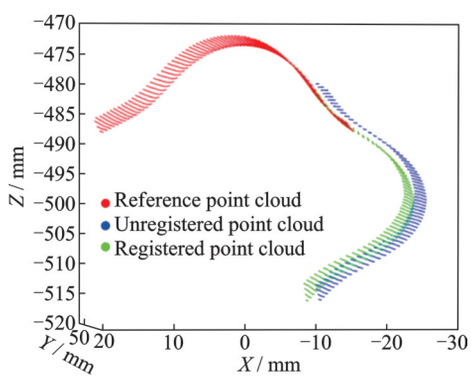

Fig.8 Point cloud matching between adjacent systems

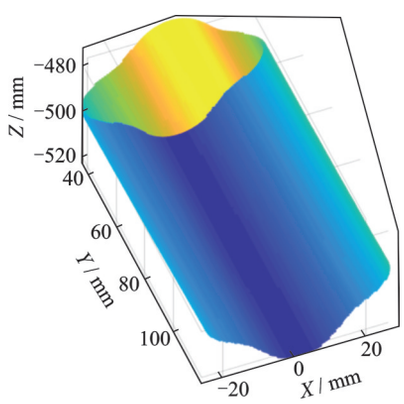

Fig.9 Corrected 3D shape diagram

The matching results of the variable curvature cylindrical shell in the initial state are compared with the reference diameter of 50.98 cm (maximum diameter) measured by a vernier caliper. Absolute error and relative error at the two-maximum diameter after rigid body calibration and point cloud matching are shown in Table 1, where 1 and 2 represent the maximum diameters of the specimen along X- and Z-axes, respectively. After point cloud matching correction, the error is significantly reduced.

Table 1 Errors at the two-maximum diameters (reference diameter: 50.98 mm)

Operation step	Maximum diameter/mm		Absolute error/mm		Relative error/%	
	1	2	1	2	1	2
Rigid body-calibration	52.15	52.67	1.17	1.69	2.30	3.31
Point cloud matching	51.11	50.66	0.13	0.32	0.26	0.63

2.2.2 360° compression measurement of the variable curvature cylindrical shell

Fig.10 and Fig.11 show the displacement and strain fields at 0, 60, 120, and 180 N, and unstable state, respectively. The unstable state occurs at approximately 190 N. As the load increased to the critical value of specimen instability, the convex region of the variable curvature cylindrical shell exhibits an S-shaped bending. Anti-symmetric protrusions and depressions developed in the concave regions on either side of the convex area. In the displacement field, the displacement distribution in the compression direction is uneven, suggesting eccentric loading during compression. When the specimen became unstable, there is a significant variation in displacement distribution at the same height of the specimen. The compressive strain of specimen increased with the load in general, but in the concave regions where protrusions occur, the stress initially increased and then decreased with the load. In the unstable state, the stress variation in the concave regions with protrusions and depressions is significantly higher than in other areas.

Fig.12 and Fig.13 are the evolution of displacement in the direction of compression and evolution of compressive strain in finite element simulation.

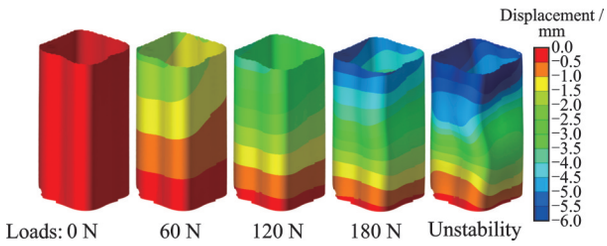

Fig.10 Evolution of displacement in the direction of compression

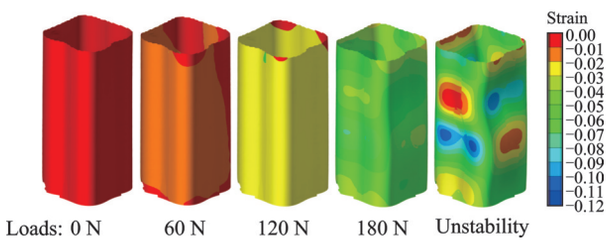

Fig.11 Evolution of compressive strain

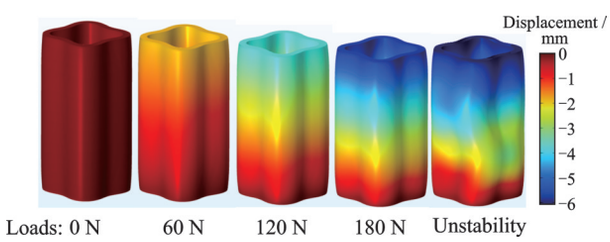

Fig.12 Evolution of displacement in the direction of compression in finite element simulation

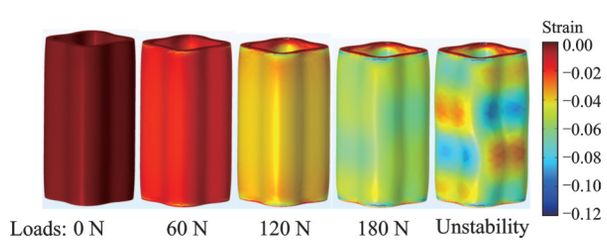

Fig.13 Evolution of compressive strain in finite element simulation

Compared with the experimental results, it can be confirmed that eccentric loading did occur during the experiment. However, as the load increased, the effect of eccentric loading gradually decreased.

3 Conclusions

A multi-camera 3D-DIC measurement system is built, which has potential advantages in measuring objects with complex geometric shapes, asymmetric deformations, or significant curvature. The camera synchronization issue is resolved using a hardware trigger mode through a synchronized con-

troller. The local coordinate systems of the multi-camera system are unified by using a multi camera calibration method based on rigid body motion. Then, through point cloud matching based on gray-scale of feature points, the transformation matrix between feature point pairs is solved using SVD method to further correct the point cloud data. 360° compression buckling measurement is carried out on variable curvature cylindrical shell, and displacement and strain nephogram of the full-surface are obtained.

References

[1] PAN Bing. Digital image correlation methods and their applications in experimental mechanics[D]. Beijing: Tsinghua University, 2007. (in Chinese)

[2] BUTLER R. Polymer composites in the aerospace industry[M]. [S.l.]: Woodhead Publishing, 2015: 77-97.

[3] PAN B. Digital image correlation for surface deformation measurement: historical developments, recent advances and future goals[J]. Measurement Science and Technology, 2018, 29(8): 082001.

[4] SPERA D, GENOVESE K, VOLOSHIN A. Application of stereo-digital image correlation to full-field 3-D deformation measurement of intervertebral disc[J]. Strain, 2011, 47: 572-587.

[5] GENOVESE K, CORTESE L, ROSSI M, et al. A 360-deg digital image correlation system for materials testing[J]. Optics and Lasers in Engineering, 2016, 82: 127-134.

[6] GUO Y P, ZHONG P, ZHUO Y, et al. Displacement field calculation of large-scale structures using computer vision with physical constraints: An experimental study[J]. Sustainability, 2023, 15(11): 8683.

[7] BADEL P, GENOVESE K, AVRIL S. 3D residual stress field in arteries: Novel inverse method based on optical full-field measurements[J]. Strain, 2012, 48(6): 528-538.

[8] HEUER F, SCHMIDT H, WILKE H J. The relation between intervertebral disc bulging and annular fiber associated strains for simple and complex loading[J]. Journal of Biomechaincs, 2008, 41(5): 1086-1094.

[9] CHEN B, PAN B. Mirror-assisted panoramic-digital image correlation for full-surface 360-deg deformation measurement[J]. Measurement, 2019, 132: 350-358.

[10] CHEN B, PAN B. Through-thickness strain field measurement using the mirror-assisted multi-view digital image correlation[J]. Mechanics of Materials, 2019, 137: 103104.

[11] TONG Z X, SHAO X X, CHEN Z N, et al. Optimization of the forearm angle for arm wrestling using multi-camera stereo digital image correlation: A preliminary study[J]. Theoretical and Applied Mechanics Letters, 2021, 11(6): 100287.

[12] WEI K, YUAN F, SHAO X X, et al. High-speed multi-camera 3D DIC measurement of the deformation of cassette structure with large shaking table[J]. Mechanical Systems and Signal Processing, 2022, 177: 109273.

[13] LI J R, YANG G B, SIEBERT T, et al. A method of the direct measurement of the true stress-strain curve over a large strain range using multi-camera digital image correlation[J]. Optics and Lasers in Engineering, 2018, 107: 194-201.

[14] CHEN B, GENOVESE K, PAN B. In vivo panoramic human skin shape and deformation measurement using mirror-assisted multi-view digital image correlation[J]. Journal of the Mechanical Behavior of Biomedical Materials, 2020, 110: 103936.

[15] ZHU K, PAN B. Panoramic/dual-surface digital image correlation measurement using a single camera[J]. Sensors, 2022, 22(9): 3266.

[16] XIE R L, CHEN B, PAN B. Mirror-assisted multi-view high-speed digital image correlation for dual-surface dynamic deformation measurement[J]. Science China Technological Sciences, 2023, 66(3): 807-820.

[17] LI J R, XIE X, YANG G B, et al. Whole-field thickness strain measurement using multiple camera digital image correlation system[J]. Optics and Lasers in Engineering, 2017, 90: 19-25.

[18] GENOVESE K, BADEL P, CAVINATO C, et al. Multi-view digital image correlation systems for in vitro testing of arteries from mice to humans[J]. Experimental Mechanics, 2021, 61(9): 1455-1472.

[19] ZHU R, JIANG D, HUANG Z X, et al. Full-field modal identification using reliability-guided frequency-domain-based digital image correlation method based on multi-camera system[J]. Measurement, 2023, 211: 112567.

[20] YANG Y H, LI K, NAWAZ M Z, et al. LED multispectral imaging based on frequency-division modulation of square wave and synchronous triggering[J]. Optik, 2022, 261: 169209.

[21] ZHANG R Z, MENG X, GARDNER L. Shape optimisation of stainless steel corrugated cylindrical shells for additive manufacturing[J]. Engineering Structures, 2022, 270: 114857.

[22] GHAZIJAHANI TG, JIAO H, HOLLOWAY D. Longitudinally stiffened corrugated cylindrical shells

under uniform external pressure[J]. Journal of Constructional Steel Research, 2015, 110: 191-199.
[23] MA H, CHEN Z P, JIAO P, et al. Numerical study on buckling behaviors of thin-walled longitudinal corrugated cylindrical shells under axial compression loads[C]//Proceedings of Pressure Vessels and Piping Conference. Las Vegas, USA: American Society of Mechanical Engineers, 2022, 83496: V002T03A056.
[24] SUN W, ZHAO J, LI X, et al. Study on the compressive properties of an elastomeric porous cylinder using 360° three-dimensional digital image correlation system[J]. Materials, 2023, 16(12): 4301.
[25] ZHANG Z Y. A flexible new technique for camera calibration[J]. IEEE Transactions on Pattern Analysis and Machine Intelligence, 2000, 22(11): 1330-1334.
[26] HUANG L, DA F P, GAI S Y. Research on multi-camera calibration and point cloud correction method based on three-dimensional calibration object[J]. Optics and Lasers in Engineering, 2019, 115: 32-41.
[27] WANG J J, ELSHEIKH A, DAVEY P G, et al. Corneal topography matching by iterative registration[J]. Proceedings of the Institution of Mechanical Engineers, Part H: Journal of Engineering in Medicine, 2014, 228(11): 1154-1167.
[28] HU T C, MA L, JIANG D, et al. Multi-camera based full-field 3D displacement measurement using digital image correlation[C]//Proceedings of 2020 13th International Symposium on Computational Intelligence and Design (ISCID). Hangzhou, China: IEEE, 2020: 164-167.
[29] CHEN X, YANG L X, XU N, et al. Cluster approach based multi-camera digital image correlation: Methodology and its application in large area high temperature measurement[J]. Optics & Laser Technology, 2014, 57: 318-326.

Acknowledgements This work was funded by the National Natural Science Foundations of China (Nos.12272176, U2037603).

Authors Mr. **LI Xin** received the B.S. degree in civil engineering from Nanjing Institute of Technology, Nanjing, China, in 2018. Since 2022, he has been pursuing a M.S. degree at Nanjing University of Aeronautics and Astronautics.
Prof. **SUN Wei** received the B.S. degree in construction engineering from Zhengzhou University, Zhengzhou, China in 2002. In 2007, she received the Ph.D. degree in Engineering Mechanics from Southeast University, Nanjing, China. Since 2007, she has been working at College of Aeronautics and Astronautics, Nanjing University of Aeronautics and Astronautics, and is currently the director of the Mechanics Center. Her research focuses on the theoretical and applied research of three-dimensional digital image related methods, as well as the static and dynamic testing methods and mechanical mechanism research of metamaterial structures.

Author contributions Mr. **LI Xin** conducted the experiment and analysis, interpreted the results and wrote the manuscript. Prof. **SUN Wei** designed the study and contributed to the discussion and background of the study. All authors commented on the manuscript draft and approved the submission.

Competing interests The authors declare no competing interests.

(Production Editor: ZHANG Huangqun)

基于多相机3D-DIC系统的变曲率圆柱壳全表面屈曲研究

李 欣, 孙 伟
(南京航空航天大学航空学院,南京 210016,中国)

摘要:为了实现变曲率物体的全表面测量,本文发展了一种360° 3D数字图像相关(Digital image correlation, DIC)系统。该测量系统由4个双相机系统组成,从多个角度拍摄物体的各表面,实现全表面完整测量。为了提高拼接质量,提出了一种逐级坐标匹配方法。首先,通过追踪三维刚体标定辅助块的运动轨迹,实现4个3D-DIC系统的初步匹配。随后,基于试件表面的特征点进行二次精确匹配。通过逐级坐标匹配方法,将每个双相机系统的相机坐标系统一到全局坐标系中,实现了变曲率圆柱壳表面的三维重构,并对结果进行了误差分析。最后进一步进行了轴向压缩屈曲实验,以测量圆柱壳表面的全场位移和应变。将实验结果与有限元结果进行了比较,验证了所提出的多相机3D-DIC测量系统的准确性和有效性。

关键词:360°三维数字图像相关;逐级坐标匹配法;全场三维变形测量;变曲率圆柱壳